



# **Numerical investigations on the rotating stall in an axial compressor and its control by flow injection at casing**

Julien Marty, Lionel Castillon, Pierric Joseph

## **► To cite this version:**

Julien Marty, Lionel Castillon, Pierric Joseph. Numerical investigations on the rotating stall in an axial compressor and its control by flow injection at casing. *Journal of Turbomachinery*, 2023, 145 (5), pp.051009. <10.1115/1.4056090>. <hal-03943765>

**HAL Id: hal-03943765**

**<https://hal.science/hal-03943765v1>**

Submitted on 17 Jan 2023

**HAL** is a multi-disciplinary open access archive for the deposit and dissemination of scientific research documents, whether they are published or not. The documents may come from teaching and research institutions in France or abroad, or from public or private research centers.

L'archive ouverte pluridisciplinaire **HAL**, est destinée au dépôt et à la diffusion de documents scientifiques de niveau recherche, publiés ou non, émanant des établissements d'enseignement et de recherche français ou étrangers, des laboratoires publics ou privés.



HAL Authorization

# Numerical investigations on the rotating stall in an axial compressor and its control by flow injection at casing

**Julien Marty\***

DAAA, ONERA

Université Paris Saclay

F-92190 Meudon - France

julien.marty@onera.fr

**Lionel Castillon**

DAAA, ONERA

Université Paris Saclay

F-92190 Meudon - France

lionel.castillon@onera.fr

**Pierric Joseph**

Univ. Lille, CNRS, ONERA, Arts et Metiers Institute of

Technology, Centrale Lille Institut, UMR 9014-LMFL,

Laboratoire de Mécanique des Fluides de Lille - Kampé

de Fériet

F-59000 Lille - France

pierric.joseph@ensam.eu

## ABSTRACT

*The operating range of a compressor is limited by surge or rotating stall line, among others. Numerical simulations must accurately predict these phenomena. This study is based on the experimental compressor CME2, which is a low-subsonic axial compressor. This compressor is tip-critical as the rotor tip is responsible for the rotating stall. This paper shows that the rotating stall onset flow rate is well captured by CFD, compared to experiments. After ten revolutions, all cells are merged and only one cell remains, as in experiments.*

*Active flow control improves compressor performance and extends the stable operating range. In the present configuration, flow injection is performed at the casing. In the simulation, the insertion of the actuators is carried out through hybrid meshes: structured mesh for blade passages and unstructured mesh for each actuator. For the some stalled operating points of baseline configuration, there is no rotating cells in the controlled configuration. Thus, the rotating stall is delayed at lower flow rate, as expected by the use of active flow control and is in agreement with the experiments.*

**KEYWORDS:** Active flow control, compressor, rotating stall, air injection

## 1. INTRODUCTION

The stable operating range of compressors used in aeronautical engines is limited by the choke line, at high flow rate, and surge line, at low flow rate. Surge and rotating stall occurring at low flow rate must be avoided for safety reasons as they can lead to the engine failure. Thus, engine manufacturers design compressors using a safety margin, called surge margin, in order to ensure a stable operating conditions at all flight conditions.

---

\* Corresponding author: Julien Marty, julien.marty@onera.fr  
Marty

Compressor design relies mainly on computational fluid dynamics. Thus, in order to accurately predict the rotating stall or surge limit, this phenomenon must be well understood. Experiments allow addressing this topic. Poesgen and Gallus [1] investigated the rotating stall of a single stage axial compressor and determined the three-dimensional pattern of a rotating-stall cell and its unsteady behavior. The onset of rotating stall depends on the tip gap size as shown by Inoue *et al.* [2] and by Hewkin-Smith *et al.* [3]. Dodds and Vahdati [4] performed static and rotating measurements and showed the coexistence of high and low cell counts and the effect of stall-rotor interaction leading to acoustic mode generation. Numerical simulations must also predict the rotating stall onset and cell development. Dodds and Vahdati [5] investigated numerically also the rotating stall in a second article. They showed that the high and low cell counts are well predicted by numerical simulations, suggesting that RANS simulations are sufficient to predict some important patterns of part-span rotating stall behavior. Marconcini *et al.* [6] investigated the rotating stall of an industrial centrifugal compressor and showed that steady simulations based on a full-annulus configuration are able to predict the operating curve and the stall onset is in good agreement with experimental value of flow coefficient. The ability of numerical simulations to predict rotating stall was also shown by Choi *et al.* [7] on a transonic fan.

Active flow control is an effective way to delay or even to suppress the rotating stall. D'Andrea *et al.* [8] investigated pulsed air injection on an axial compressor and showed that the hysteresis loop associated to rotating stall can be removed. Margalida *et al.* [9] succeeded in delaying rotating stall via flow injection at casing, upstream of the rotor and deeply investigated on the onset mechanism of rotating stall and its modification by active flow control. Weigl *et al.* [10] stabilized rotating stall using active feedback control based on twelve air injectors and showed that, injecting 3.6% of the designed compressor mass flow reduces up to 11% the stalled mass flow. Bae *et al.* [11] studied also the active flow control of tip clearance flow in a linear cascade with three kinds of actuators. More recently, Ashrafi *et al.* [12] delayed the rotating stall inception using an annular plasma actuator based on dielectric barrier discharge.

Most studies rely on experiments. Few research works are based on numerical simulations to investigate the effect of active flow control on rotating stall inception and development. Marty *et al.* [13] studied several flow control techniques to improve the stall margin of a compressor, but focused mainly on passive flow control such as axisymmetrical grooves, non-axisymmetrical slots, or even recirculation approach. The work of Halawa *et al.* [14] aimed at optimizing the efficiency of stall control in centrifugal compressor using air injection and showed that an injection of 1.5% of inlet mass flow rate at 30 degrees delays the stall onset from 4 to 3.8 kg/s. The investigation of Gmelin *et al.* [15] relies on a linear cascade and the use of steady, pulsed or synthetic jets to control corner separation via slots located at the endwall or at the blade suction side. They found an excellent agreement between experiments and simulations in terms of control effectiveness.

The objective of this paper is to study the impact of active flow control on the rotating stall onset of an axial compressor, thanks to steady and unsteady RANS simulations. More precisely, this paper aims at investigating the ability of CFD to capture the one-stall-cell pattern on the axial compressor and the delay of stall onset due to the active flow control. This requires an accurate prediction of the rotating stall onset and evolution of stall cells. The paper is organized as follows: first, the experimental test bench is described and then, the numerical setup is detailed. Numerical results are analyzed in two steps: validation of numerical setup on the baseline configuration (without active flow control) and effect of injected flow on rotating stall onset and evolution.

## 2. MATERIALS AND METHODS

### 2.1 Experimental setup

The test case considered in this study is the CME2 axial compressor located at Arts et Métiers (Lille, France). This is a low speed, single stage machine representative to a high-pressure compressor of an aero-engine in terms of stage loading [16]. Table 1 summarizes the main geometrical characteristics and some flow properties for the rotational speed considered in this study.

**TABLE 1:** CME2 COMPRESSOR MAIN CHARACTERISTICS

Rotational speed (rpm)	3200
Design mass flow rate (kg/s)	5.3
Design axial velocity, LE (m/s)	43
Rotor blade number	30
Stator blade number	40
Casing diameter (mm)	550
Hub-tip ratio, LE	0.75
Rotor tip chord (mm)	84
Rotor tip stagger angle (°)	54
Rotor tip gap (mm)	0.5

A dedicated test bench using a 200 kW electric motor and a speed multiplier allows operating the compressor and setting the requested rotational speed. A throttling vane is located after the compressor. It allows moving its working point along its performance curve up to the stall inception. The entrance of the circuit consists in a tranquilization chamber followed by a converging section, allowing also the measurement of the mass flow rate through the stage. Figure 1 depicts the whole installation. One particularity of this setup is to be able to perform repeated stall tests and to operate in rotating stall regime without any damages thanks to its moderate pressure ratio and to its mechanical robustness.

As an experimental tool, this test bench hosts a complete and modular set of instrumentation. It is relevant here to mention a first differential pressure sensor (First Sensor BTEM50025) allowing measuring the mass flow rate at the converging section and another

one, a First Sensor BTEM50350, devoted to the pressure increase between rotor inlet and stator outlet. One estimates the measurement uncertainties of this setup to  $\pm 0.012 \text{ kg.s}^{-1}$  and  $\pm 1.3 \text{ Pa}$  after in house calibration [9].

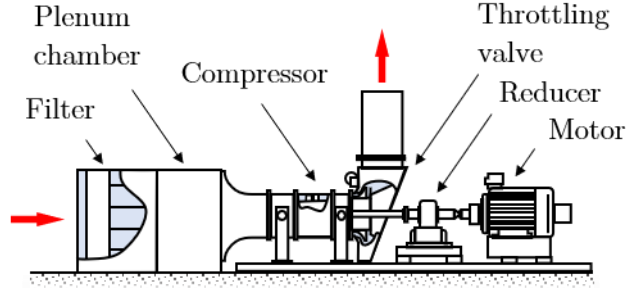


**FIGURE 1:** CME2 COMPRESSOR AND ASSOCIATED TEST BENCH [9]

To complete the description of the experimental setup, it is worth mentioning that this test bench includes a complete active flow control with pulsed jets [9]. This particular setup used 20 slots machined all around the casing of the compressor, each slot hosting a pair of pulsed jets (i.e. 40 jets in total). Each pulsed jet consists in an actuator (a Matrix 820 magnetic valve, rated to 180 nL/min and 500 Hz maximum), paired with a Coandă shaped nozzle with a  $10 \times 0.5 \text{ mm}^2$  slot (see Figure 2). Each injector is located 10 mm upstream the rotor leading edge, and is able to rotate along its axis with  $15^\circ$  steps. Thanks to the valves characteristics, up to 2.5% additional mass flow rate can be added to the main flow with near sonic velocity. Each injection block is spaced by  $13^\circ$ , and in a given block, injectors are spaced by  $5^\circ$  (see Figure 3).

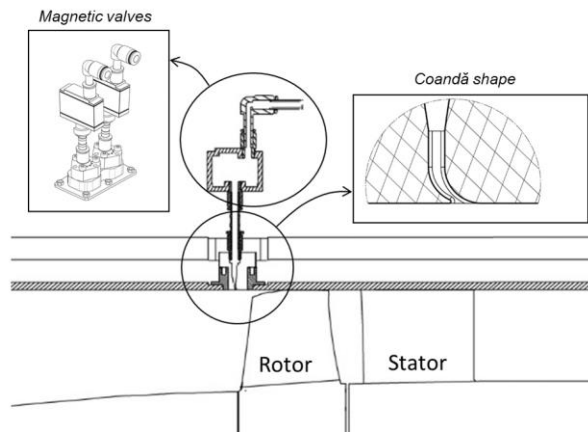


**FIGURE 2:** AXIAL POSITIONING AND COMPOSITION OF PULSED JETS

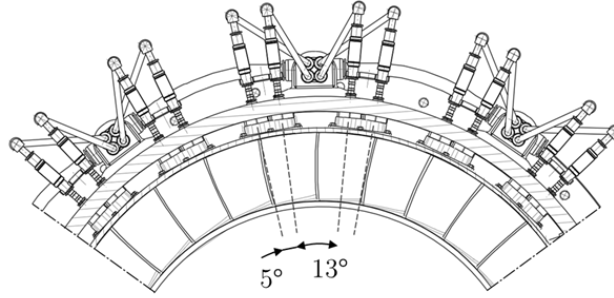


**FIGURE 3:** ANGULAR ARRANGEMENT OF THE PULSED JETS AROUND THE CASING

## 2.2 Numerical setup

The numerical simulations presented in this article have been accomplished using ONERA's CFD software *elsA* [17][18][19], which has been developed since 1997 and is co-owned by ONERA and SAFRAN. *elsA* is a multi-application aerodynamic code based on a cell-centered finite volume method for structured and unstructured meshes. Solving the compressible, three-dimensional RANS equations, *elsA* allows simulating a wide range of aerospace configurations such as aircrafts, space launchers, missiles, helicopters and turbomachines. Therefore a wide range of numerical tools, turbulence models and boundary conditions are available. In the past few years, an important work has allowed the extension of the multi-block structured solver in *elsA* to an hybrid grid solver, in which structured (ijk-based) and unstructured blocks may coexist within the same computational domain [20]. Structured zones may be kept for the sake of efficiency and of accuracy in viscous layers, whereas unstructured zones may enable an easier mesh generation and adaptation process. The latest improvements have been achieved by the work of Soismier [21].

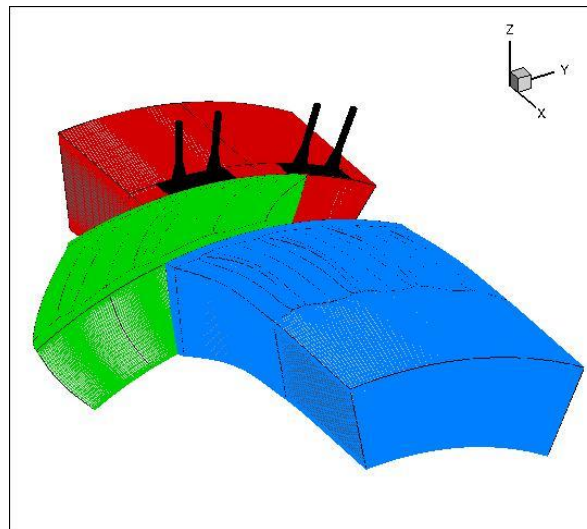


**FIGURE 4:** MESH OF THE CME2 COMPRESSOR (1/10TH OF THE CIRCUMFERENCE). GLOBAL VIEW OF THE 3 ROWS

In order to compute URANS computations of the CME2 configuration with the injectors at the casing, two different grids are considered. The first grid is a mesh corresponding to  $1/10^{\text{th}}$  of the circumference ( $36^\circ$ ), as illustrated in Figure 4. Indeed, the blade counts of the compressor (30 rotors, 40 stators) and the number of injectors (20 couples) enable to perform such computational domain reduction in order to reduce the computational cost, especially for the computations of the stable operating points of the compressor map. This first mesh includes 50 blocks and 15 million cells. The second grid is the one used for the computations of operating points in the unstable region of the compressor map. Since the flow is no more periodic in space and in time, it is necessary to use a full annulus grid, obtained by duplicating ten times the previous mesh in order to reach a  $360^\circ$  sector, leading to a grid composed of almost 500 blocks and 150 million cells. The non dimensionalised wall cell ( $y^+$ ) is less than 1, and a grid sensitivity analysis had been previously performed [22] on this compressor case, showing that grid independency is obtained and that the current grid is acceptable.

The two types of grid are “hybrid”, in the sense that they allow both structured and unstructured parts. As illustrated in the close up view in see Figure 5, the mesh of the channels (upstream part in red, rotor part in green, and stator part in blue) is meshed with structured blocks using a classical “O-nH” topology, while the mesh of the injectors is meshed with unstructured blocks. Indeed, due to the complexity of the shape of the injectors, the use of unstructured elements, such as tetrahedra, pyramids, prism and hexahedra eases the mesh generation. The unstructured blocks of the injector (in black) are connected to the structured mesh of the upstream cylindrical channel (in red) thanks to conformal matching boundaries. Figure 6 represents close up views of the 5 meshes of the injectors corresponding to the 5 different injections angles ( $\alpha_{\text{inj}}$ ) which are investigated :  $-30^\circ, -15^\circ, 0^\circ, +15^\circ$  and  $30^\circ$ . In the schematic view, the green rectangle represents the injection angle equal to zero. The flow is injected from the left to the right, that is to say, the flow direction is aligned with the rotational axis in the blade-to-blade view.

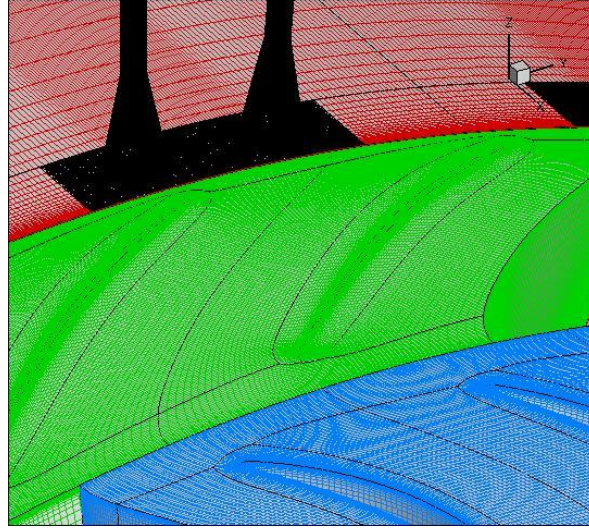


**FIGURE 5:** MESH OF THE CME2 COMPRESSOR (1/10<sup>th</sup> OF THE CIRCUMFERENCE). CLOSE UP VIEW AT THE CASING ZONE

As reminded in [23], this “hybrid” grid approach offers several advantages. First of all, it requires much less effort compared to a full structured multiblock grid generation, which can be time expensive and in some cases impossible. Moreover, compared to a full unstructured grid approach, the hybrid grid approach has the advantage of keeping the “O-nH” type grid topology (well adapted to turbomachinery flows) in most of the part of the blade channel. One last advantage of this approach is that the conformal matching between the structured and non-structured zones avoids any conservation loss issue, which can be encountered with the Chimera technique [24], or flow filtering issues, which can appear with mismatched abutting interface techniques.

RANS and URANS numerical simulations are performed on the two computational grids using the upwind scheme of Roe [25] associated to the MUSCL “minmod” limiter. The Harten coefficient value is set as small as possible ( $\Psi_{\text{Roe}}=0.01$ ) in order to be at the same time robust and as little dissipative as possible. The first order accurate Backward-Euler scheme is used for time integration, coupled to an LU implicit phase. For the URANS computations, the physical time step has a value close to  $1\mu\text{s}$  corresponding to 18,000 time steps to perform a single rotation. Previous study [22] showed that the chosen time step values enables a satisfactory capture of the main unsteady phenomenon, in particular the rotating stall phenomena. The one equation Spalart-Allmaras model [26] is used for turbulence, previous studies having shown its ability to capture rotating stall phenomenon [27].



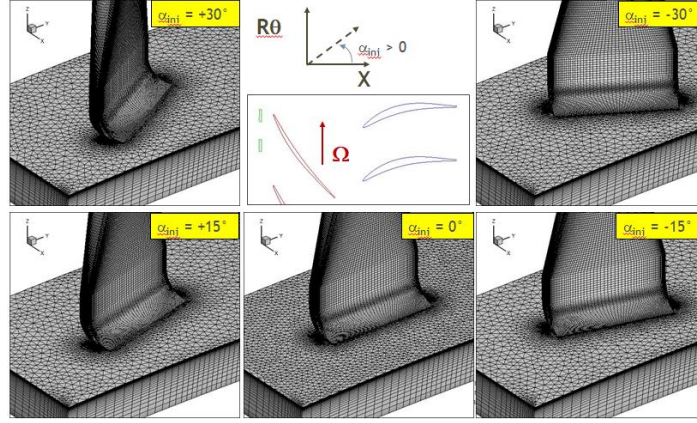


**FIGURE 6:** CLOSE UP VIEW OF THE INJECTOR GRID FOR THE DIFFERENT ANGLES OF INJECTION

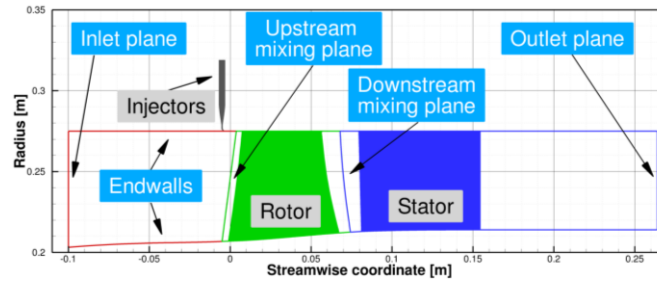


**FIGURE 7:** SCHEMATIC VIEW OF BOUNDARY CONDITION LOCATIONS.

Concerning the boundary conditions, their locations are depicted in Figure 7, especially inlet/outlet planes and mixing planes. At the inlet of the computational domain an axial flow direction is imposed with uniform values for the stagnation temperature (288 K) and stagnation pressure (101,325 Pa). At the inlet of the injectors (maximum radius location of the black injector domains on Figure 4), atmospheric stagnation temperature (288 K) and mass-flow are imposed (2g/s for each injector, corresponding to 80 g/s for the whole circumference, which is close to 2% of the stall mass flow rate). For these two inlet boundaries, very low levels of turbulent quantities are imposed (close to 0). Some of the calculations are accomplished without any injection through the injectors, by keeping the domains of the injectors and replacing the injection condition with a solid wall treatment on the upstream frontier of the injectors at the maximum radius location. Adiabatic wall conditions are imposed on all of the walls (blades, casing, hub, injector walls). Finally, downstream of the computational domain, a subsonic outlet condition is used in which the static pressure is imposed with a radial equilibrium law, the downstream pivot static pressure used for the radial equilibrium law integration being defined through a valve law ( $P_s = P_{ref} + \alpha_{relax} (Q/Q_{ref})^2$ ), where  $Q$  is the massflow at the outlet boundary and  $(\cdot)_{ref}$  values are reference values for static pressure and massflow. This means that for each operating point, the parameter  $\alpha_{relax}$  is modified in order to change the target mass-flow and the associated operating

point (the mass-flow decreases as the  $\alpha_{\text{relax}}$  parameter increases. The steady computations are accomplished using a mixing plane treatment while it is replaced by a sliding joint condition for the URANS computations. The position of the rotor/stator interfaces is located between the three blade rows, as highlighted in Figure 5, with the three different rows represented respectively in red, green and blue.

### 3. RESULTS AND DISCUSSION

#### 3.1 Baseline configuration

The first step of this study consists in evaluating the ability to predict the rotating stall limit of the CME2 compressor by comparison to experimental data. This is performed through the calculation of the static pressure rise at casing, across the stage, between planes located 73 mm upstream and 225 mm downstream of the rotor leading edge, respectively. The static pressure is then averaged in the circumferential direction as simulations are performed in relative frame. Figure 8 shows the evolution of static pressure rise coefficient along with the flow coefficient. The experimental values are compared with different RANS calculations (performed on different computational domains) and with the URANS computation (performed on the  $360^\circ$  sector). Experimentally, the rotating stall of compressor occurs at a flow coefficient of 0.4. The stall onset is relative to sudden drop of the static pressure rise coefficient, as shown by the blue arrow. First steady RANS simulations based on one single blade channel (SBC) are able to predict this operating limit (green line). The computational domain of these simulations is not prepared to receive the active flow control device, as the red part is  $2\pi/30$ -periodic instead of  $2\pi/20$ -periodic, and thus, they do not contain the upstream mixing plane between red and green parts in Figure 5 and in Figure 7. These simulations capture well the stall onset. Nonetheless, due to the presence of injectors, which are similar to a fixed row, the upstream mixing plane is required and this influences the static pressure rise by delaying the rotating stall occurrence up to 0.36 and by decreasing the level of static pressure rise over the stable operating range. As a result, the discrepancy in terms of stall onset with experiments comes from the added mixing plane that acts as a boundary condition placed very close to the rotor and not from the solver ability to capture the rotating stall. Similar results are obtained with  $1/10^{\text{th}}$  of the circumference, up to the stall limit. Small discrepancies appear beyond this limit as the difference in terms of periodic conditions ( $1/10^{\text{th}}$  vs. single blade channel) leads to different boundary conditions and the converged steady state differs. Four operating points are simulated over the full-annulus configuration (steady RANS and unsteady RANS). Results are similar to previous numerical data, in the stable operating range. Once the rotating stall occurs, discrepancies are observed and can be explained by an insufficient time length used to compute time averaged flow.

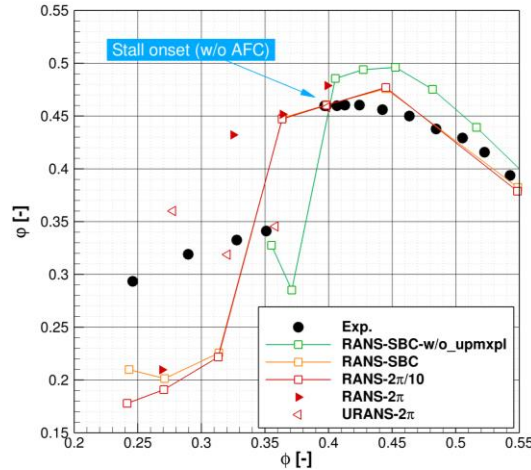


**FIGURE 8:** STATIC PRESSURE RISE ACROSS THE COMPRESSOR STAGE FOR THE BASELINE CONFIGURATION

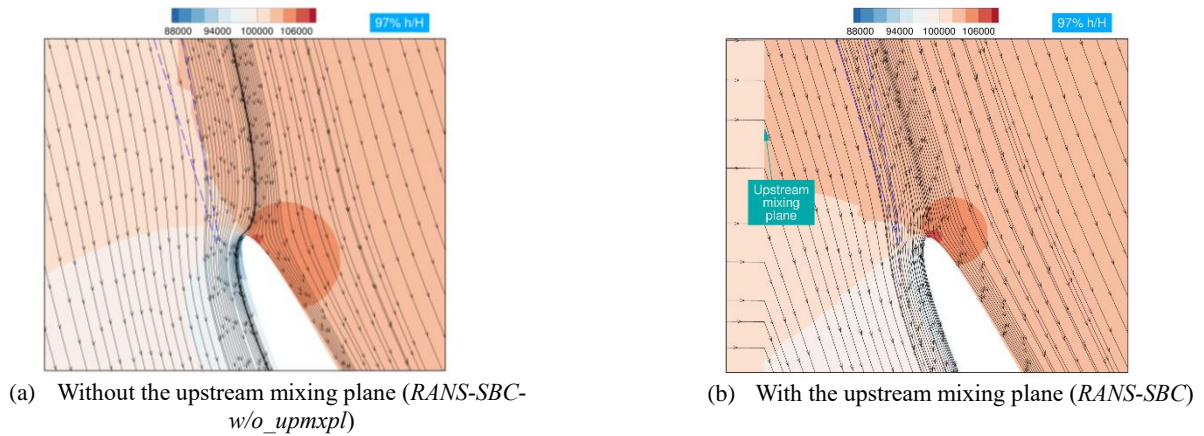


**FIGURE 9:** STATIC PRESSURE CONTOURS AND STREAMLINES IN RELATIVE FRAME AROUND THE ROTOR LEADING EDGE

In order to explain discrepancies between RANS simulations with a single blade channel, without and with the upstream mixing plane, *RANS-SBC\_w/o\_upmxpl* and *RANS-SBC* configurations, respectively, Figure 9 depicts the static pressure field and streamlines computed in the relative frame, at 97% of the relative height in spanwise direction (100% is relative to the casing wall), for the flow coefficient equal to 0.44. Two blue dashed lines are used as lines of reference to make the comparison easier. The comparison of both simulations shows that, as the upstream mixing plane is located in the potential effect of the rotor, this affects the angle of attack viewed by the rotor. The purely axial flow allowed by the presence of the upstream mixing plane is observed closer to the rotor and is not influenced by the static pressure field around the rotor. This leads to a significant effect on the angle of attack. With the upstream mixing plane, this angle is smaller. Thus, this explains why the stall onset occurs at a lower flow coefficient.

Before analyzing the influence of the active flow control, it is important to highlight the occurrence of the rotating stall in the compressor. Experimentally, the rotating stall occurs at the rotor tip and only one cell is observed on the static pressure measurements [9]. Figure 10 depicts the time evolution of the entropy variation across the compressor, from an initial field which is the steady state obtained by RANS simulations. The contours are shown at 90% spanwise, at four different instants (after 1, 3, 5 and 10 revolutions after the start of the unsteady simulation), for the time-averaged flow coefficient of 0.36. Figure 11 depicts, with the same scale, the entropy variation in the rotor/stator axial interface plane. The evolution of entropy rise highlights the alignment of tip leakage vortex to the rotor leading edge plane and the appearance of rotating stall cells. After one revolution, the periodicity of the flow is lost and high loss areas are observed near the tip, close to the trailing edge. These are the footprints of separation in each rotor channel. After three revolutions, ten cells are observed and they are not periodic, some rotor channels being blocked, and others not. The blockage due to stall cell creates an incidence rise on the adjacent blade, leading to stall. As each cell covers a different azimuthal extent and their rotating velocities differ allowing an interaction between rotating stall cells. The low velocity zones created by stall cells rotate in the circumferential direction and gradually tend to merge as they rotate with the rotor blades, leading to two main cells after five revolutions, and a single cell after ten revolutions. Thus, five additional revolutions are necessary to switch from two to one cell. It should be noticed, that, at the flow coefficient 0.4, there is no rotating cell, in the full-annulus simulation (URANS) as shown in Figure 12. After stabilization of the simulation, the flow is still periodic and no separation occurs at the tip. For the other operating points, the higher the throttle is, the faster separations occur and rotating cells merge.

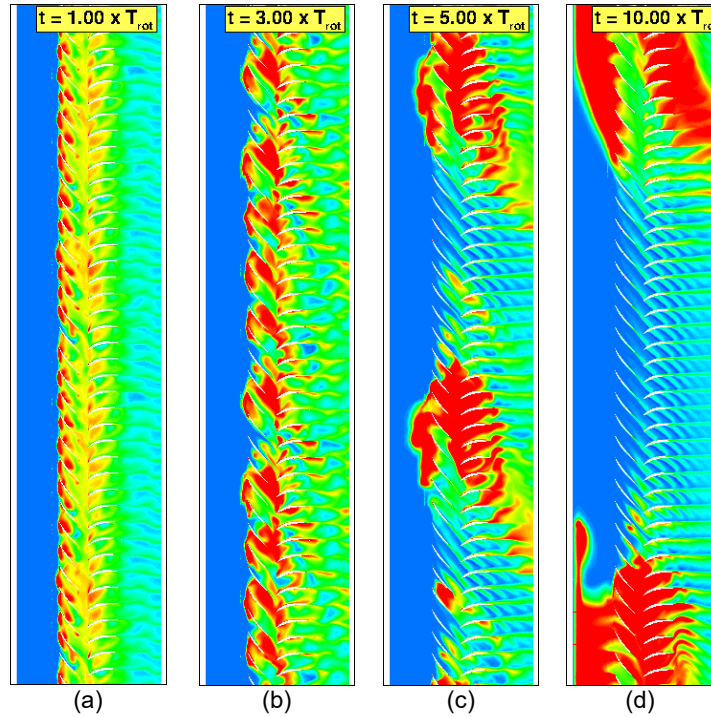


**FIGURE 10:** ENTROPY VARIATION FIELD AT 90% SPAN AT THE FLOW COEFFICIENT  $\phi=0.36$ , FOR THE FULL ANNULUS CONFIGURATION

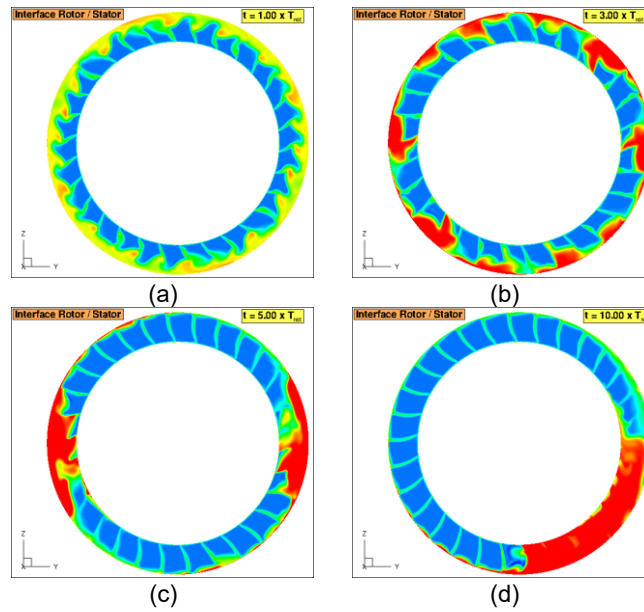


**FIGURE 11:** ENTROPY VARIATION FIELD DOWNSTREAM OF THE ROTOR, AT THE FLOW COEFFICIENT OF  $\phi=0.36$ , WITH THE FULL-ANNULUS CONFIGURATION

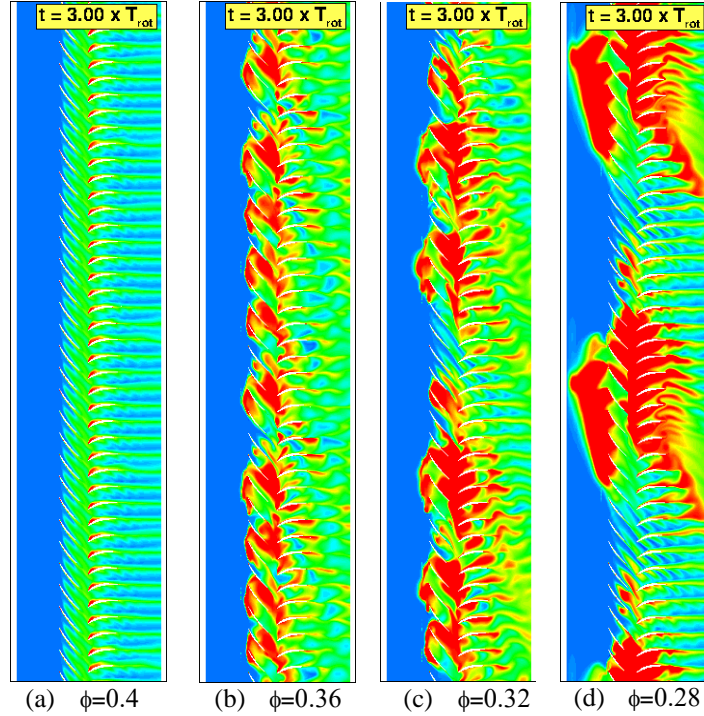


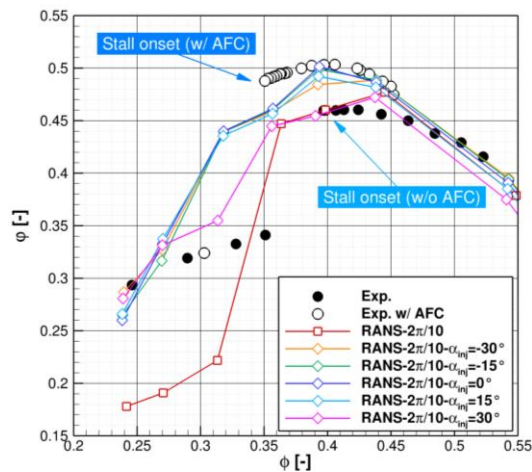
**FIGURE 12:** ENTROPY VARIATION FIELD AT 90% SPAN FOR THE FULL ANNULUS CONFIGURATION, AT FOUR DIFFERENT OPERATING POINTS

### 3.2 Impact of active flow control

As shown before, injectors are added with hybrid meshes. RANS simulations are carried out on the 1/10<sup>th</sup> configuration for all orientations of the injector (Figure 13). The injected mass flow rate, in standard condition, is 2g/s for each injector, that is to say 80g/s for the full-annulus (less than 2% of the mass flow at the rotating stall onset). The experimental data with active flow control based on an axial injection ( $\alpha_{inj}=0^\circ$ ) is included in the graph. The agreement between numerical results and experimental data is good in the stable operating range. However, the static pressure drop occurs too early in the simulations. Figure 14 depicts the static pressure rise coefficient for the rotor, the stator and the stage. This shows that the first decrease of static pressure rise is not due to the stall on the rotor but on a static pressure drop across the stator. Figure 15 depicts the wall streamlines over rotor and stator suction sides and shows that a corner separation over stator suction side occurs before the stall onset over the rotor blade. This too spread separation over the stator suction side at the casing junction with the casing is responsible for the first decrease of static pressure rise coefficient.

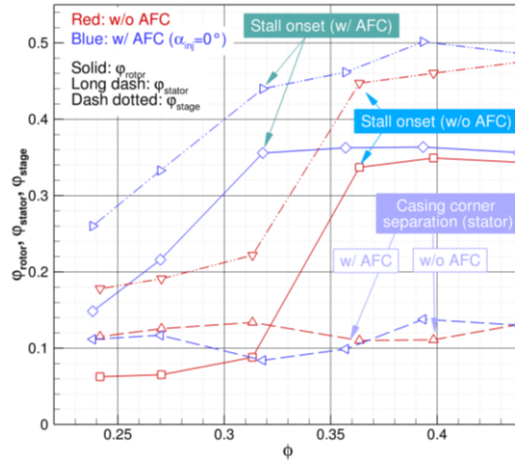
In the stable operating range (flow coefficient higher than  $\phi=0.4$ ), the active flow control does not significantly influence the static pressure rise coefficient across the compressor stage, the only exception being the  $30^\circ$  angle. The effect of injected flow is clearly visible once the rotating stall occurs in the baseline configuration. The reduction of static pressure rise coefficient is delayed to lower flow coefficient as the maximum value reaches  $\phi=0.47$  at  $\phi=0.39$  instead of  $\phi=0.46$  at  $\phi=0.44$ . For lower flow coefficient, the static pressure

rise coefficient remains higher than 0.44 up to  $\phi=0.32$  before a sudden drop. By comparison to the baseline configuration, the drop is delayed from  $\phi=0.36$  to  $\phi=0.32$ , which is similar to the delay observed on the maximum static pressure rise coefficient. This variation (0.04) is close to the experimental shift of the stall onset (0.05). The effect of the injector orientation is small by comparison to the adding of active flow control in the computational domain. This is due to the use of the mixing plane between injectors (similar to a fixed row) and rotors, which averages the flow in the azimuthal direction. Far from injectors in circumferential direction, injected massflow does not influence the flow orientation. Thus, the flow remains axial in the absolute frame. As the injected flow covers partially the azimuthal extent, this zero angle reduces the area-averaged flow angle due to the mixing plane and finally viewed by the rotors. The mixing plane tends to minimize the effect of flow angle. Thus, unsteady simulations are required to compute more accurately the effect of injector angle. Nevertheless, as this study aims at investigating the effect of flow control on rotating stall, these unsteady simulations are only carried out with the axial injection angle ( $\alpha_{inj}=0^\circ$ ).

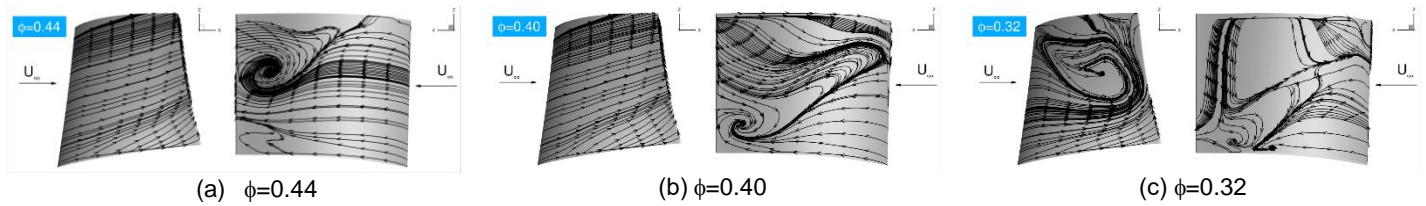


**FIGURE 13:** STATIC PRESSURE RISE ACROSS THE COMPRESSOR STAGE FOR THE CONTROLLED CONFIGURATIONS WITH DIFFERENT INJECTOR ORIENTATIONS





**FIGURE 14:** STATIC PRESSURE RISE ACROSS THE ROTOR, THE STATOR AND THE STAGE FOR THE 1/10<sup>TH</sup> SECTOR CONFIGURATION, WITHOUT AND WITH ACTIVE FLOW CONTROL



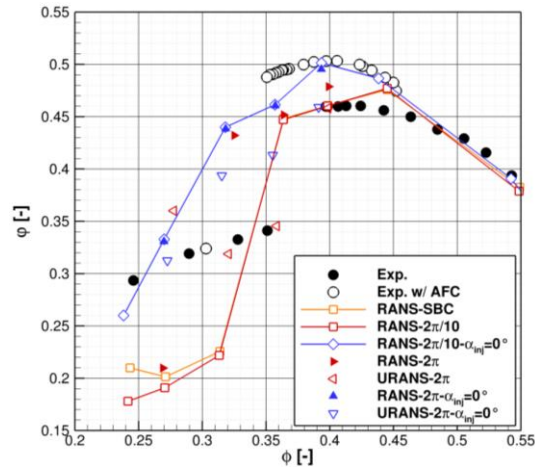
**FIGURE 15:** WALL STREAMLINES OVER THE ROTOR (LEFT) AND STATOR (RIGHT) SUCTION SIDES AT THREE OPERATING POINTS, FOR THE CONFIGURATION WITHOUT ACTIVE FLOW CONTROL.

Figure 16 and Figure 17 show the static pressure rise coefficient of the baseline configuration and of the controlled configuration with the zero angle orientation. Computations on controlled configuration are carried out for the 1/10<sup>th</sup> sector and for full-annulus. Unsteady simulations are only performed on the latter one. Numerical results of baseline configuration are also recalled (single blade channel, 1/10<sup>th</sup> and full-annulus). The static pressure drop is delayed and reduced by adding the active flow control. This effect is seen quite consistently on the three different types of computations: steady calculations on the 1/10<sup>th</sup> mesh, steady and unsteady computations on the full-annulus mesh. Yet the full annulus unsteady computations tend to predict a lower pressure drop than the steady computations. Thus, RANS simulation are slightly pessimistic. It should be noticed that length of time signal is insufficient for the time average computation. Thus, these operating points are given for information only.

Figure 18 depicts the entropy variation field at 90% span, after five revolutions for baseline (top) and controlled (bottom) configurations. The initial field is still a steady RANS simulation based on mixing plane at the rotor-stator interface. The four operating points are the same as in Figure 12:  $\phi=0.4$ , 0.36, 0.32 and 0.28, from left to right, respectively. At stable operating point, the flow is periodic in the baseline configuration while the active flow controls leads to a slight loss of periodicity without any impact on stall limit. The flow is certainly different from one passage to another, but there is no sign of blockage in each passage. Thus, the compressor



operates at a stable regime. By throttling the compressor (decrease of mass flow rate), discrepancies between baseline and controlled configurations are more and more observable. At the flow coefficient 0.36, rotating cells are visible on the baseline configuration. The default of periodicity is still present in the controlled configuration and is accentuated by areas of high and low entropy variation alternately. Separations and blockage occur over one or two passages and the one or two next passages are not subjected to these phenomena thanks to the flow injected at casing. Thus, after five revolutions, there is no rotating cells at this mass flow rate while the baseline configuration is stalled. At flow coefficients, 0.32 and 0.28, two rotating cells are visible on the entropy variation field but their development is slowed down by the injected flow. The active flow control delays the rotating stall onset and pushes back the stable operating limit. It should be noticed that the drop of static pressure rise is directly linked to the appearance of the rotating stall cells.



**FIGURE 16:** STATIC PRESSURE RISE ACROSS THE COMPRESSOR STAGE FOR THE BASELINE CONFIGURATION AND CONTROLLED CONFIGURATION WITH ZERO INJECTOR ANGLE

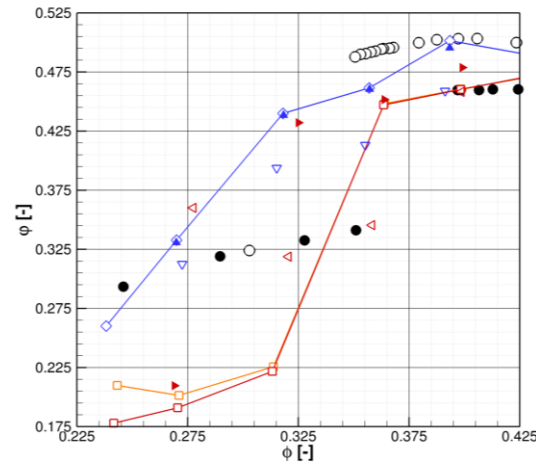


**FIGURE 17:** STATIC PRESSURE RISE ACROSS THE COMPRESSOR STAGE IN THE UNSTABLE REGIME (FLOW COEFFICIENT LOWER THAN 0.4)

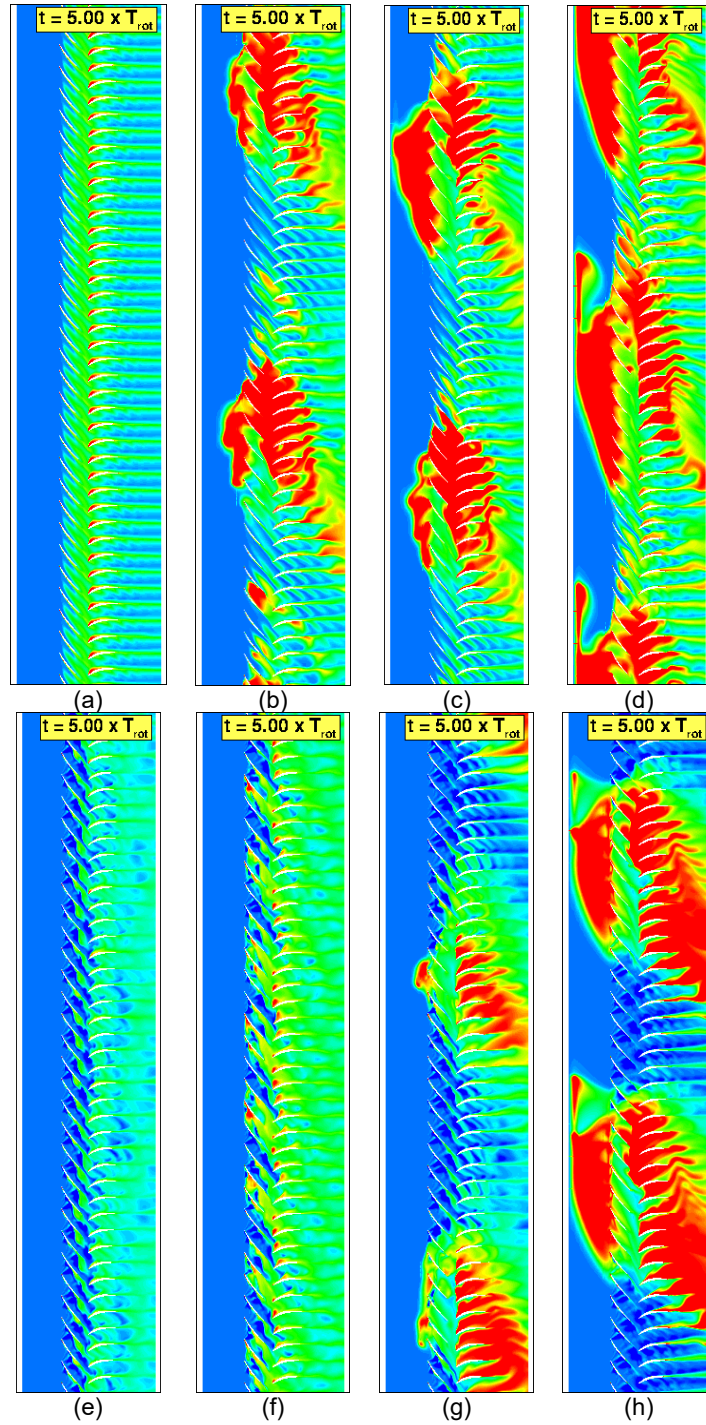


**FIGURE 18:** ENTROPY VARIATION FIELD AT 90% SPAN AT FOUR DIFFERENT OPERATING POINTS AND FOR BASELINE (TOP) AND CONTROLLED (BOTTOM) CONFIGURATIONS (FULL ANNULUS CONFIGURATION)

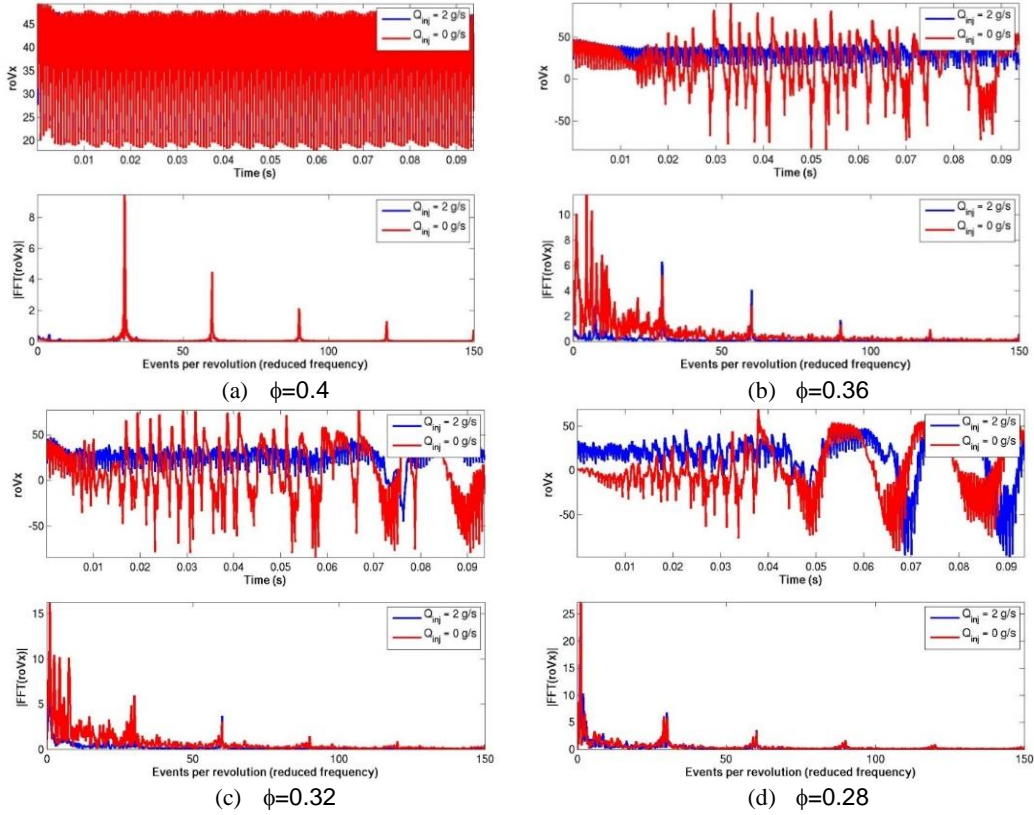


**FIGURE 19: COMPARISON OF AXIAL MOMENTUM SIGNALS (TIME/FREQUENCY DOMAINS, H/H=90%)**

In order to highlight the delay of stall onset, time signal analysis is performed for all full-annulus computations. Figure 19 shows the axial momentum signal recorded on a gauge located in the absolute frame of reference on the rotor/stator interface at 90% of span height. All signals are plotted both in time and frequency domain thanks to the use of Fast Fourier Transform. The red and blue signals correspond respectively to the case without and with injection. The frequency domain allows the identification of particular frequencies, such as the rotor passing frequency as the gauge is then located downstream of the rotor: 30 events per revolution are directly linked to the rotor blade number (30).

For the first shown operating point ( $\phi=0.4$ ), the flow is stable for both configurations (without and with active flow control) and the existing frequencies correspond as expected to the rotor blade passing frequencies and its harmonics (30 blades). For the second operating point ( $\phi=0.36$ ), rotating stall occurs in the baseline configuration, which explains the appearance of a large spectrum of low frequencies: the flow periodicity is broken and the time evolution is no more driven by the blade passing frequencies. On the contrary, although some low frequencies are visible on the spectrum due to the periodicity loss, the configuration with active flow control remains stable and has a Fourier spectrum close to the one of a stable operating point. This is no longer the case for the third operating point ( $\phi=0.32$ ) for the simulation with flow injection at casing since the injection does not delay anymore the onset of rotating stall cells.

However the time signals plotted in, Figure 19-c show that the appearance of instabilities is delayed with the injection. Rotating stall occurs after 10 ms without active flow control and after 60 ms with injectors. Thus, in a real compressor, even if active flow control cannot remove indefinitely the stall onset, this increase the available time between a possible precursor detection and stall onset in order to avoid the latter. Finally, for the last operating point, a low frequency corresponding to two events per revolution is clearly highlighted and corresponds to the two rotating cells observed after five revolutions. The time signal analysis is thus coherent with the previous analysis of the entropy variation field.

#### 4. CONCLUSION

The present numerical study focuses on the rotating stall in the axial compressor CME2 and its control. The active flow control corresponds to flow injection at casing thanks to twenty pairs of injectors and based on the Coandă effect in order that the injected flow remains close to the endwall. The injected mass flow rate is smaller than 2% of the mass flow rate at stall onset.

The comparison to experimental data, from single blade channel to  $1/10^{\text{th}}$  to full-annulus configurations, validates the numerical setup. The rotating stall is well captured by steady RANS CFD despite the delay due to the presence of a mixing plane between injectors and rotors.

The analysis of the baseline configuration shows that the rotor is tip-critical as separations occur at blade tip. Moreover, there is an alignment of tip leakage vortex with the rotor leading edge, leading to the compressor stall. For the present compressor, ten revolutions are required to capture the stall pattern composed of one rotating stall cell. Five revolutions are necessary to switch from two to one cell.

Active flow control does not influence significantly the static pressure rise across the compressor. Nevertheless, as expected, it delays the drop of static pressure rise, which is a sign of occurrence of rotating stall and emergence of stall cells. Both steady and unsteady RANS simulations predict this drop, even if steady computations are slightly pessimistic. Even if this statement can be configuration-dependent, the drop is well captured by steady RANS computations over a reduced computational domain ( $1/10^{\text{th}}$  in the present case thanks to the spatial periodicity).

In the present study, the rotating stall onset is delayed at least from the flow coefficient 0.4 to 0.36, as rotating stall cells are visible at  $\phi=0.32$  for the controlled configuration. This observation performed on entropy variation field at 90% span is corroborated by the analysis of axial momentum signals recorded by a gauge at the same channel height. Moreover, active flow control slows down the development of rotating stall cells. This statement will be verified experimentally. If confirmed, thanks to tip injection, the slow-down of rotating stall would increase available response time to avoid the stall onset once precursors are detected.

As the effect of injector angle is only investigated on the 1/10<sup>th</sup> configuration with steady RANS simulations, which rely on the use of a mixing plane at the rotor-stator interface, this effect will be studied with unsteady simulations on the full-annulus configuration, as further works. This is mandatory to fully validate the capacity of the numerical setup to predict the effect of flow injection at casing.

A future publication will present the power balance of the flow control system. Preliminary analyses of the on-going tests on the CME2 compressor show that flow injection saves energy for certain operating points.

## ACKNOWLEDGEMENTS

All simulations have been performed in the framework of the elsA agreement between SAFRAN and ONERA, which are co-owners of this software. This paper is funded by European Union's Horizon 2020 research and innovation program under grant agreement No 886352, project ACONIT.

## NOMENCLATURE

RANS	Reynolds-Averaged Navier-Stokes
URANS	Unsteady Reynolds-Averaged Navier-Stokes
$P_s, P_{ref}$	Static pressure, reference pressure
$Q, Q_{ref}$	Mass-flow, reference mass-flow
$\alpha_{relax}$	Valve coefficient
$\alpha_{inj}$	Injection angle of the injector device
$\varphi$	Static pressure rise coefficient [ $\Delta P_s / (\rho U^2)$ ]
$\phi$	Flow coefficient [ $(Q / \rho A) / U$ ]

## REFERENCES

- [1] Poensgen, C. A., and Gallus, H. E., “Rotating Stall in a Single-Stage Axial Flow Compressor.” ASME. J. Turbomach. 118(2): pp 189–196, 1996, <https://doi.org/10.1115/1.2836625>.
- [2] Inoue, M., Kuroumaru, M., Yoshida, S., and Furukawa, M., “Short and Long Length-Scale Disturbances Leading to Rotating Stall in an Axial Compressor Stage With Different Stator/Rotor Gaps.” ASME. J. Turbomach; 124(3): 376–384, July 2002. <https://doi.org/10.1115/1.1458022>.

- [3] Hewkin-Smith, M., Pullan, G., Grimshaw, S. D., Greitzer, E. M., and Spakovszky, Z. S., “The Role of Tip Leakage Flow in Spike-Type Rotating Stall Inception.” ASME. J. Turbomach.; 141(6): 061010, June 2019. <https://doi.org/10.1115/1.4042250>.
- [4] Dodds, J., and Vahdati, M., “Rotating Stall Observations in a High Speed Compressor - Part I: Experimental Study.” ASME. J. Turbomach.; 137(5): 051002, May 2015. <https://doi.org/10.1115/1.4028557>.
- [5] Dodds, J., and Vahdati, M. “Rotating Stall Observations in a High Speed Compressor - Part II: Numerical Study.” ASME. J. Turbomach.; 137(5): 051003, May 2015. <https://doi.org/10.1115/1.4028558>.
- [6] Marconcini, M., Bianchini, A., Checcucci, M., Ferrara, G., Arnone, A., Ferrari, L., Biliotti, D., and Rubino, D. T., “A Three-Dimensional Time-Accurate Computational Fluid Dynamics Simulation of the Flow Field Inside a Vaneless Diffuser During Rotating Stall Conditions.” ASME. J. Turbomach.; 139(2): 021001, February 2017. <https://doi.org/10.1115/1.4034633>.
- [7] Choi, M., Smith, N. H. S., and Vahdati, M., “Validation of Numerical Simulation for Rotating Stall in a Transonic Fan.” ASME. J. Turbomach.; 135(2): 021004, March 2013. <https://doi.org/10.1115/1.4006641>.
- [8] D’Andrea, R., Behnken, R. L., and Murray, R. M., “Rotating Stall Control of an Axial Flow Compressor Using Pulsed Air Injection.” ASME. J. Turbomach.; 119(4): 742–752, October 1997. <https://doi.org/10.1115/1.2841184>.
- [9] Margalida, G., Joseph, P., Roussette, O., and Dazin, A., “Active Flow Control in an Axial Compressor for Stability Improvement: On the Effect of Flow Control on Stall Inception.” Exp. Fluids, 62(1), p. 12, 2021. <https://doi.org/10.1007/s00348-020-03104-4>.
- [10] Weigl, H. J., Paduano, J. D., Fréchette, L. G., Epstein, A. H., Greitzer, E. M., Bright, M. M., and Strazisar, A. J., “1997 Best Paper Award—Controls and Diagnostics Committee: Active Stabilization of Rotating Stall and Surge in a Transonic Single-Stage Axial Compressor.” ASME. J. Turbomach. ; 120(4): 625–636, October 1998. <https://doi.org/10.1115/1.2841772>.
- [11] Bae, J. W., Breuer, K. S., and Tan, C. S. “Active Control of Tip Clearance Flow in Axial Compressors.” ASME. J. Turbomach.; 127(2): 352–362, April 2005. <https://doi.org/10.1115/1.1776584>.
- [12] Ashrafi, F., Michaud, M., and Duc Vo, H. “Delay of Rotating Stall in Compressors Using Plasma Actuators.” ASME. J. Turbomach; 138(9): 091009, September 2016. <https://doi.org/10.1115/1.4032840>.
- [13] Marty, J., Castillon, L., Boniface, J.-C., Burguburu, S., Godard, A., “Numerical and Experimental Investigations of Flow Control in Axial Compressors”. Aerospace Lab, Alain Appriou, 2013, p. 1-13. <https://hal.archives-ouvertes.fr/hal-01184639/document>.
- [14] Halawa, T., Gadala, M. S., Alqaradawi, M., and Badr, O., “Optimization of the Efficiency of Stall Control Using Air Injection for Centrifugal Compressors.” ASME. J. Eng. Gas Turbines Power.; 137(7): 072604, July 2015. <https://doi.org/10.1115/1.4029169>.

- [15] Gmelin, C., Zander, V., Hecklau, M., Thiele, F., Nitsche, W., Huppertz, A., and Swoboda, M.. “Active Flow Control Concepts on a Highly Loaded Subsonic Compressor Cascade: Résumé of Experimental and Numerical Results.” ASME. J. Turbomach.; 134(6): 061021, November 2012. <https://doi.org/10.1115/1.4006308>.
- [16] Day, I. J., “Stall, Surge, and 75 Years of Research,” J. Turbomach., 138(1), 011001, January 2016. <https://doi.org/10.1115/1.4031473>.
- [17] Cambier L., Gazeix, M. “elsA: an efficient object-oriented solution to CFD complexity”. 40th AIAA Aerospace Science Meeting & Exhibit, Reno, USA, 2002
- [18] Cambier, L., Veuillot, J.P., “Status of the elsA CFD Software for the Flow Simulation and Multidisciplinary Applications”, 48th AIAA Aerospace Science Meeting & Exhibit, 2008
- [19] Cambier, L., Heib S., Plot S., “The Onera elsACFD software: input from the research and feedback from industry”, Mechanics and Industry; 14, 159-174, AFM, EDP Sciences 2013, <https://doi.org/10.1051/meca/2013056>.
- [20] de la Llave Plata, M., Couaillier, V., Le Pape, M.C., Marmignon, C., “elsA-Hybrid: an all-in-one structured/unstructured solver for the simulation of internal and external flows. Application to turbomachinery”. 4th EUCASS Conf. Saint-Petersburg, 2011
- [21] Soismier, M., Corre, C., Castillon, L., Marmignon, C., “Improvements in the multiblock hybrid CFD solver elsA-H for turbomachinery flow simulation”, Proceedings of the 12th International Symposium on Experimental and Computational Aerothermic of Internal Flows.
- [22] Baretter, A., Godard, B., Joseph, P., Roussette, O., Romanò, F., Barrier, R., Dazin, A., “Experimental and Numerical Analysis of a Compressor Stage under Flow Distortion”, International Journal of Turbomachinery, Propulsion and Power, doi:10.3390/ijtpp6040043, <https://www.mdpi.com/2504-186X/6/4/43>
- [23] Castillon, L., Soismier, M., Le Pape, M.C., Maugars, B., Michel, B., “A hybrid structured/non structured grid strategy for the CFD modeling of technological effects on complex Turbomachinery applications.”, ISABE 2019, Canberra, Sept. 2019
- [24] Castillon, L., Billonnet, G., Riou, J., Péron, S., Benoit, C., “A Technological Effect Modeling on Complex Turbomachinery Applications With an Overset Grid Numerical Method”, Journal of Turbomachinery, October 2014, 136(10):101005. <https://doi.org/10.1115/1.4027997>.
- [25] Roe, P. L., “Approximate Riemann solvers, parameter vectors and difference schemes”, J. Comput. Phys., 43 (2):357-372, October 1981. [https://doi.org/10.1016/0021-9991\(81\)90128-5](https://doi.org/10.1016/0021-9991(81)90128-5).
- [26] Spalart, P. R. and Allmaras, S. R., “A One-Equation Turbulence Model for Aerodynamic Flows.” La Recherche Aérospatiale, No. 1, 1994, pp. 5-21.

[27] Gourdain, N., Burguburu S., Leboeuf F., Miton H., “Numerical Simulation of Rotating Stall in a Subsonic Compressor”, Aerospace Science and Technology, Vol 10, p9-18, 2006